# Magnetic Damping Modulation in $IrMn_3/Ni_{80}Fe_{20}$ via the Magnetic Spin Hall Effect

José Holanda[1,*] Hilal Saglam,[1,2,3] Vedat Karakas,[4] Zhizhi Zang[1,5] Yi Li,[1] Ralu Divan,[6] Yuzi Liu,[6]
Ozhan Ozatay,[4] Valentine Novosad,[1] John E. Pearson[1] and Axel Hoffmann[1,7]

[1]*Materials Science Division, Argonne National Laboratory, Lemont, Illinois 60439, USA*
[2]*Department of Physics, Illinois Institute of Technology, Chicago, Illinois 60616, USA*
[3]*Department of Applied Physics, Yale University, New Haven, Connecticut 06511, USA*
[4]*Physics Department, Bogazici University, North Campus, Bebek/Istanbul 34342, Turkey*
[5]*School of Optical and Electronic Information, Huazhong University of Science and Technology,
Wuhan 430074, People's Republic of China*
[6]*Center for Nanoscale Materials, Argonne National Laboratory, Argonne, Illinois 60439, USA*
[7]*Department of Materials Science and Engineering, University of Illinois at Urbana-Champaign,
Urbana, Illinois 61801, USA*

Noncollinear antiferromagnets can have additional spin Hall effects due to the net chirality of their magnetic spin structure, which provides for more complex spin-transport phenomena compared to ordinary nonmagnetic materials. Here we investigated how ferromagnetic resonance of permalloy ($Ni_{80}Fe_{20}$) is modulated by spin Hall effects in adjacent epitaxial $IrMn_3$ films. We observe a large dc modulation of the ferromagnetic resonance linewidth for currents applied along the [001] $IrMn_3$ direction. This very strong angular dependence of spin-orbit torques from dc currents through the bilayers can be explained by the magnetic spin Hall effect where $IrMn_3$ provides novel pathways for modulating magnetization dynamics electrically.

Antiferromagnetic materials are promising for future spintronic applications, since they combine several advantages. They are robust against perturbation due to magnetic fields, produce no stray fields, display ultrafast dynamics, and are capable of generating large magnetotransport effects [1,2]. The idea of using antiferromagnetic materials in spintronic devices [1–4] has gained interest with the realization that antiferromagnets can be efficient sources of spin currents [5–12] and that their spin structure can be modulated electrically. Furthermore, antiferromagnets with noncollinear spin configurations provide additional rich new spin-transport phenomena, since any chirality of their spin structure may result in nonvanishing Berry curvatures affecting profoundly their charge transport properties [13–15]. Towards this end, it has been shown that triangular antiferromagnets with chiral spin arrangements can exhibit ferromagneticlike behaviors such as large anomalous Hall and Nernst effects, as well as a magneto-optical Kerr effect. An interesting addition to these discoveries is the magnetic spin Hall effect (MSHE) in the triangular antiferromagnet $Mn_3Sn$ [16]. The origin of the MSHE is similar to that of the ordinary spin Hall effect (OSHE), however, the MSHE arises from a reactive counterpart of the dissipative spin response that gives rise to OSHE. This interpretation can be understood in terms of the symmetries of linear response functions that are supported here by the dependence of the spin Hall effect (SHE) signals on the magnetic-order

parameter reversal. This means that the MSHE can be explored under the condition of ferromagnetic resonance and represents a new way of analyzing the magnetization dynamics, i.e., when dc electrical current passes through the uniformly magnetized material, a nonequilibrium distribution of spins at the interface influences the dynamic properties. In particular, current-induced modulation of damping has become a standard technique for quantifying spin Hall effects [17,18]. Therefore, the control of damping in ferromagnetic or antiferromagnetic bilayers can provide fundamental insights for ferromagnetic or antiferromagnetic spintronics.

An interesting material to be investigated is the noncollinear antiferromagnet $IrMn_3$, in which Mn atoms form kagome lattice in the {111} planes [See Fig. 1(a)]. $IrMn_3$ has a giant magnetocrystalline anisotropy energy due to the locally broken cubic symmetry of the Mn sublattices [19]. Additionally, $IrMn_3$ has a large variation of the spin Hall conductivities along different crystallographic orientations [20–22]. In this Letter, we perform ferromagnetic resonance measurements without and with dc current in $IrMn_3/Ni_{80}Fe_{20}$ bilayers. Our results show a strong angular dependence of the electric current induced modulation of the ferromagnetic resonance linewidth for magnetic fields applied along different crystalline orientations, i.e., [001] and [011]. We report a maximum Gilbert damping modulation of 41% and the observed anisotropy for the magnetic
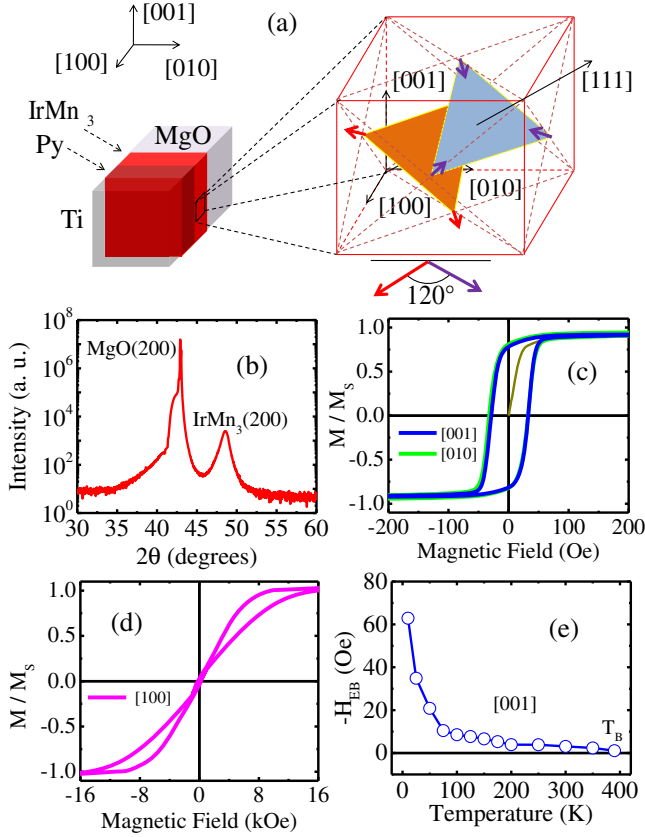
FIG. 1. (a) The schematic of the $IrMn_3/Ni_{80}Fe_{20}$ (permalloy, Py) bilayer capped with a thin layer of Ti and also the unit cell of $IrMn_3$ with its spin structure. Note that the Mn atoms in the unit cell of $IrMn_3$ form a kagome lattice in the {111} planes with the spins either pointing inwards or outwards in each triangular Mn arrangement. (b) The x-ray diffraction pattern measured for a 20-nm thick $IrMn_3$ layer capped with a 2-nm Ti layer. (c) Measured magnetic hysteresis curves after field cooling in a magnetic field of $+70$ kOe applied along either the [001] or [010] directions at a temperature of 300 K. (d) Magnetic hysteresis curves after field cooling in a magnetic field of $+70$ kOe applied along the [100] direction at a temperature of 300 K. (e) Measured exchange bias field as a function of temperature after field cooling with an applied magnetic field of $+70$ kOe along the [001] direction, showing that the blocking temperature of the $IrMn_3(20\ nm)/Ni_{80}Fe_{20}(10\ nm)$ bilayer is 380 K.

fields applied along the two different crystalline directions can be associated with the variation of spin accumulation at the interface due to the additional contributions arising from the magnetic spin Hall effect.

We have grown nominally 20-nm thick epitaxial $IrMn_3$ films on MgO (100)-oriented single-crystal substrates at 843 K using a magnetron sputtering technique. Subsequently, a thin layer of $Ni_{80}Fe_{20}(10\ nm)$ and Ti (2 nm) were deposited at room temperature. Here, the Ti layer was used to protect the surface properties of $Ni_{80}Fe_{20}$. Figure 1(a) shows the unit cell of $IrMn_3$, where the Mn moments are parallel to the {111} planes and aligned along

the $\langle 112 \rangle$ directions. Figure 1(b) shows an x-ray diffraction pattern for $IrMn_3$ grown on a MgO substrate. We found that $IrMn_3$ has a lattice constant of $(0.377 \pm 0.001)$ nm, which is consistent with previous literature values [20,23].

The magnetic characterization was performed with a superconducting quantum interference device (SQUID) magnetometer. Figures 1(c)–1(e) are measured for MgO/ $IrMn_3(20\ nm)/Ni_{80}Fe_{20}(10\ nm)/Ti(2\ nm)$. In Figures 1(c) and 1(d) we show the hysteresis curves at room temperature (300 K) after field cooling starting at temperature of 390 K with a magnetic field of $+70$ kOe applied along the crystallographic directions [001], [010], and [100]. From the SQUID measurements we also determine a saturation magnetization of $M_S = (774 \pm 8)$ emu/cm$^3$, which is consistent with typical values reported for permalloy [16]. Figure 1(e) shows the exchange bias field as a function of temperature for magnetic fields applied along the [001] direction, where exchange bias is defined as $H_{EX} = -(H_1 + H_2)/2$. This means that the blocking temperature is above 300 K, which shows that $IrMn_3$ is antiferromagnetically ordered at room temperature [23].

We utilize a flip-chip ferromagnetic resonance technique [24] for characterizing the Gilbert damping measured for fields applied in different crystal orientations. We measured the transmission coefficient by sweeping the frequency at fixed fields. Figure 2(a) shows the experimental configuration for ferromagnetic resonance measurements without and with dc currents. Figures 2(b) and 2(e) show the ferromagnetic resonance (FMR) signals obtained with a vector network analyzer (VNA) for magnetic fields applied along the [001] and [011] crystallographic directions, respectively. For the measurements with the magnetic field along [011] the sample is rotated 45° with respect to the coplanar waveguide and thus not symmetrically positioned, which may give rise to the slight asymmetric line shape observed in Fig. 2(e).

Figures 2(c) and 2(f) show the measured FMR frequency as a function of the magnetic field. The solid curve is a fit of the experimental data to the Kittel equation, $f = \gamma[(H_R) (H_R + 4\pi M_{eff})]^{1/2}$, where $\gamma = g\mu_B/\hbar = 2.8$ GHz/kOe is the gyromagnetic ratio, $g = 2$ is the spectroscopic splitting factor, $\mu_B$ is the Bohr magneton, $\hbar$ the reduced Planck constant, and $4\pi M_{eff}$ the effective magnetization, which is determined by the fit $4\pi M_{eff} = (9706 \pm 1)$ Oe, consistent with the SQUID data. As expected, there is no significant variation in the ferromagnetic resonance field for single $Ni_{80}Fe_{20}$ or $Ni_{80}Fe_{20}/IrMn_3$ samples. The frequency swept linewidths ($\Delta f_{VNA}$) were obtained via Lorentz fitting. Detailed steps, including the conversion from $\Delta f_{VNA}$ to resonance magnetic field linewidth $\Delta H$ can be found in Ref. [24]. The linewidth as a function of the frequency is given by $\Delta H = (\alpha/\gamma)f$ [25], where $\alpha$ is the magnetic Gilbert damping of the material. Figures 2(d) and 2(g) show the linewidth and fits are made using $\Delta H = (\alpha/\gamma)f$. The damping values for both crystallographic directions
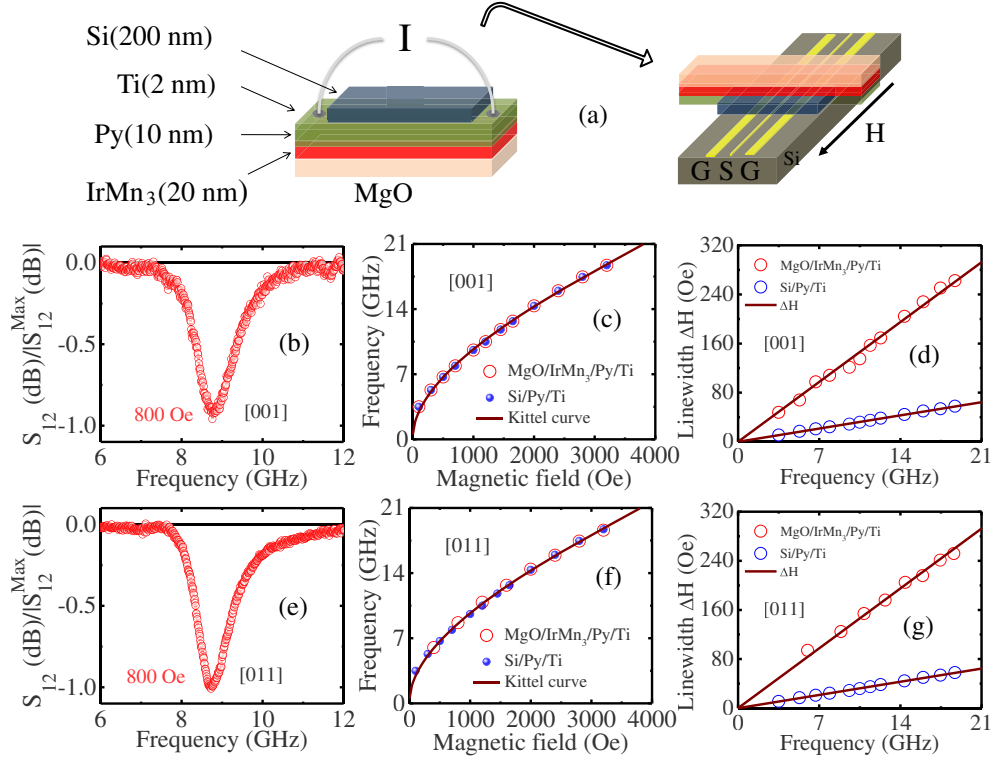
FIG. 2. (a) Schematic of the flip-chip ferromagnetic resonance measurement setup, where dc current (I) leads are connected to the Ti layer. (b) and (e) ferromagnetic resonance (FMR) signals obtained using a VNA for the magnetic field applied along the [001] and [011] crystallographic directions, respectively. (c) and (f) FMR frequency as a function of magnetic field, which was applied along the [001] and [011] crystallographic directions, respectively. The fits are performed with the Kittel equation, where $\gamma = g\mu_B/\hbar = 2.8$ GHz/kOe and $4\pi M_{\text{eff}} = (9706 \pm 1)$ Oe. (d) and (g) The linewidth variation as a function of the FMR frequency for the crystallographic directions [001] and [011], respectively.

[001] and [011] are practically the same $\alpha_{\text{IrMn}_3/\text{Py}} = (3.94 \pm 0.02) \times 10^{-2}$, but damping increased significantly in comparison to a single layer of $\text{Ni}_{80}\text{Fe}_{20}(\text{Py})$ $\alpha_{\text{Py}} = (8.66 \pm 0.03) \times 10^{-3}$. Using the variation of the damping, it is possible to determine the spin-mixing conductance $g_{\text{eff}}^{\uparrow\downarrow} = 4\pi M_{\text{eff}} t_{\text{FM}} \Delta\alpha/(\gamma\hbar) = (1.6 \pm 0.1) \times 10^{16}$ cm$^{-2}$ [19], where $t_{\text{FM}} = 10$ nm is the thickness of the ferromagnetic material ($\text{Ni}_{80}\text{Fe}_{20}$, Py).

The experimental results with applied dc currents along the [001] direction are shown in Fig. 3 and suggest that there are three distinct contributions to $\alpha$: the first, current-independent mechanism is that $\alpha$ is strongly facet dependent and is derived from the antiferromagnetic domains of the uncompensated spins; the second, magnetic field-independent mechanism is facet independent and arises from bulk spin-orbit coupling within the IrMn$_3$ layer, and the third mechanism, which is both magnetic field direction and electric current dependent, is the magnetic spin Hall effect (MSHE). It is known that chemically ordered IrMn$_3$ has a triangular chiral magnetic structure with the Mn magnetic moments aligned at 120° to each other in the (111) plane [20]. The coupling of the magnetization of $\text{Ni}_{80}\text{Fe}_{20}$ to the Mn interface moments becomes strongly fixed in its
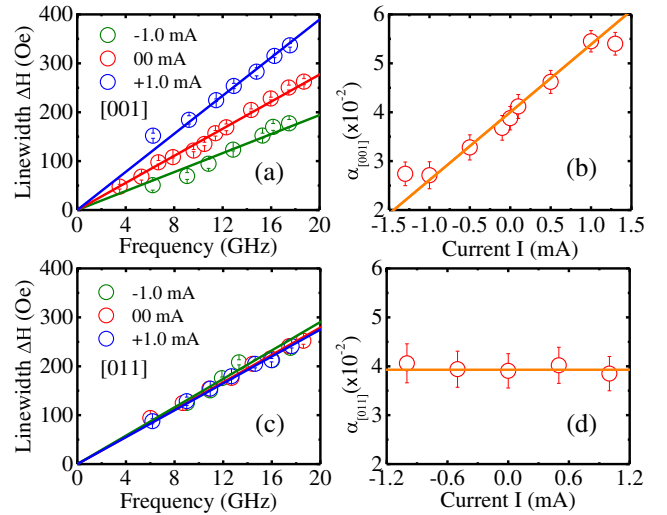


FIG. 3. Electric current modulation of FMR measured for MgO/IrMn$_3$(20 nm)/Ni$_{80}$Fe$_{20}$(10 nm)/Ti(2 nm). (a) and (c) FMR linewidth variation as a function of the resonance frequency with dc currents of $\pm 1$ mA applied along the [001] crystallographic direction and magnetic field applied along the [001] and [011] crystallographic directions, respectively. (b) and (d) Damping variation as a function of dc current for the [001] and [011] crystallographic directions, respectively.

preferred direction [26–28] by the preferred antiferromagnetic domains in the bulk of the IrMn$_3$ film. The coupling at the IrMn$_3$/Ni$_{80}$Fe$_{20}$ interface is responsible for the spin current flow and the concomitant manipulation of damping of the magnetization in Ni$_{80}$Fe$_{20}$. Figures 3(a) and 3(c) show the linewidth variation as a function of the resonance frequency for the magnetic field applied along the [001] and [011] crystallographic directions, respectively. Based on the Landau-Lifshitz-Gilbert-Slonczewski equation the linewidth as a function of the frequency can be written as $\Delta H = \alpha f/\gamma + \theta_{MSH}^{eff}\hbar j_c L/(2eM_{eff}t_{FM})$, where $\theta_{MSH}^{eff}$ is the effective magnetic spin Hall angle, $e$ is the charge of electron, $j_c$ is the charge density, and the spin transparency of the interface is represented by $L = [g_{eff}^{\uparrow\downarrow} \tan(t_{AFM}/2\lambda_{AFM})]/[\sigma h/(2\lambda_{AFM}e^2) + g_{eff}^{\uparrow\downarrow} \coth(t_{AFM}/\lambda_{AFM})]$ [29], where $\lambda_{AFM}$ is the spin diffusion length in the IrMn$_3$, $g_{eff}^{\uparrow\downarrow}$ is the effective spin mixing conductance, $\sigma$ is the electrical conductivity, and $t_{AFM}$ is the thickness of the IrMn$_3$. For analyzing the measurements of the IrMn$_3$(20 nm)/Py(10 nm) samples with the magnetic field applied along the [001] direction we used the following parameters: resonance frequency $f = (17.45 \pm 0.03)$ GHz, linewidth of $\Delta H = (336.5 \pm 0.5)$ Oe, dc current density of $j_c = 2.5 \times 10^4$ A cm$^{-2}$, the spin diffusion length $\lambda_{AFM} = 1$ nm [20], thickness $t_{AFM} = 20$ nm, and electrical conductivity $\sigma_{[001]}^{Elec} = (8.2 \pm 0.2) \times 10^3$ $\Omega^{-1}$ cm$^{-1}$, which is in accordance with the previously reported values [20–22]; using these parameters we obtain an effective magnetic spin Hall angle of $\theta_{MSH}^{eff} \sim (0.33 \pm 0.02)$. This result is consistent with Ref. [20], where the spin Hall effect was probed via other techniques.

We observe that for the magnetic field applied along the [001] direction a change in the magnetic damping occurs, depending on the direction (positive or negative) of the applied dc current. This does not occur when the magnetic field is applied along the [011] direction, which indicates a change of the current induced torques in Ni$_{80}$Fe$_{20}$ as a function of the magnetic field due to the MSHE of IrMn$_3$. Also note that the electrical conductivity of Ni$_{80}$Fe$_{20}$ is $\sigma_{Py} = 2 \times 10^4$ $\Omega^{-1}$ cm$^{-1}$ [30] and thus $\sigma_{Py}/\sigma_{[001]}^{Elec} = (2.4 \pm 1)$. Together with the thickness ratio of the two layers, this means that the dc current flows in about equal parts through the Ni$_{80}$Fe$_{20}$ and IrMn$_3$ layers. At the same time Ni$_{80}$Fe$_{20}$ has a small spin Hall angle, $\theta_{SH} = 0.005$ [31] compared to IrMn$_3$ (i.e., $\theta_{SH}/\theta_{MSH}^{eff} \approx 1.5\%$) and thus any magnetic torques originating from electric current flowing through the Ni$_{80}$Fe$_{20}$ layer can be neglected. Figures 3(b) and 3(d) show the variation of the magnetic damping of the Ni$_{80}$Fe$_{20}$ layer as a function of the applied dc current along the crystallographic [001] direction and the magnetic field applied in crystallographic [001] and [011] directions, respectively.

The MSHE generated in IrMn$_3$ leads to significant changes in the magnetization dynamics of the adjacent Ni$_{80}$Fe$_{20}$ layer depending on the crystalline orientations. For a (100)-oriented IrMn$_3$ film, the in-plane current leads to a large out-of-plane spin current whose amplitude is much larger than that of a (111)-oriented IrMn$_3$ films [20]. In IrMn$_3$, the Mn atoms are arranged in the form of triangles within the {111} planes of the primitive crystallographic unit cell, such that the Mn moments point either toward (spins-in) or away from the center of the triangle (spins-out), respectively [see Fig. 4(a)]. Using either a mirror reflection or time-reversal operation, the spins-in
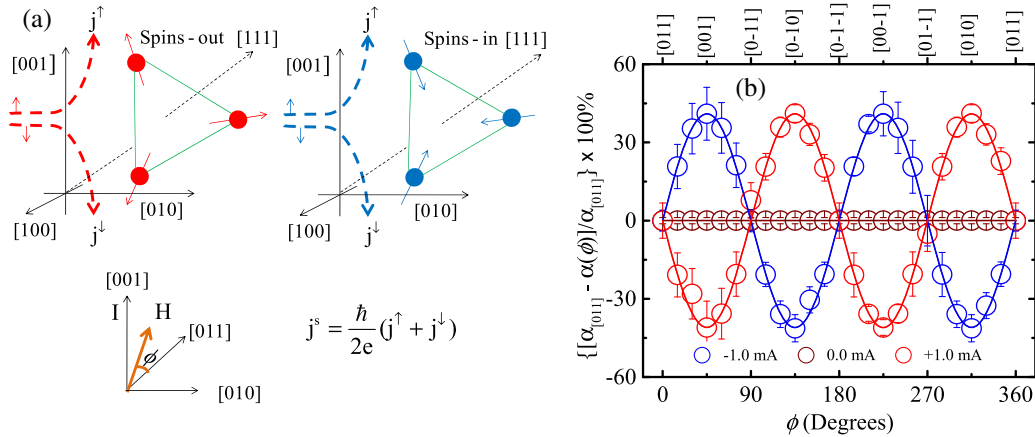


FIG. 4. (a) Schematic diagram of two chiral antiferromagnetic spin configurations (spins-in and spins-out) of the Mn moments in IrMn$_3$. Because of the magnetic spin Hall effect, the trajectories of spin-up and spin-down electrons have opposite transverse components and produce a spin current in the [001] direction. The angular variation of the magnetic field ($H$) in the plane of the film is also shown and it determines the polarization of the spin accumulation due to the magnetic spin Hall effect. (b) Variation of the current dependent Gilbert magnetic damping as a function of the applied magnetic field angle, which in turn defines the polarization of the spin accumulation due to the magnetic spin Hall effect. The curves represent the function $\{[\alpha_{[011]}-\alpha(\varphi)]/\alpha_{[011]}\} \times 100\% = \Delta\alpha_{MSHE} \sin(\pm 2\varphi)$, with $\Delta\alpha_{MSHE} = (40 \pm 1)\%$.

and spins-out configurations can be transformed into each other. For example, for the (011)-crystallographic plane, the reversal operation process should apply to both the lattice and the magnetic moments and thus time reversal reverses the directions of all moments, because either the mirror symmetry or the time-reversal symmetry is broken in $IrMn_3$. On the other hand, spins-in and spins-out are nonequivalent ground states and are chiral images of each other. In this case, the spins-in and spins-out configurations exhibit the same energies and both exist spontaneously in the material [32,33]. It is known that under time reversal the magnetic spin Hall effect is odd [16], whereas the conventional spin Hall effect is even [31]. Thus, we can conclude with the help of time reversal that both spin configurations will exhibit the same MSHE, as schematically shown in Fig. 4.

Figure 4(b) shows for a $MgO/IrMn_3(20\ nm)/Ni_{80}Fe_{20}(10\ nm)/Ti(2\ nm)$ sample the damping variation as a function of the applied magnetic field angle, which in turn defines the polarization of the spin accumulation due to the magnetic spin Hall effect. The modulation of the electric current induced damping modulation of the $Ni_{80}Fe_{20}$ as a function of the applied magnetic field direction provides an efficient pathway for modulating magnetization dynamics. The influence of the spin accumulation generated by the spin current $j^s = (j^\uparrow + j^\downarrow)\hbar/2e$ at the $IrMn_3/Ni_{80}Fe_{20}$ interface due to the MSHE also depends on the crystallographic direction of the sample. As shown in Fig. 3(a) for $-1$ or $+1$ mA dc current, the damping variation for magnetic fields applied either along the [001] or [011] crystallographic directions is $\Delta\alpha_{MSHE} \approx (40 \pm 1)\%$. This result was also confirmed by the data in Fig. 4(b). The fit of Fig. 4(b) was realized with the function $\{[\alpha_{[011]} - \alpha(\varphi)]/\alpha_{[011]}\} \times 100\% = \Delta\alpha_{MSHE}$ $\sin(\pm 2\varphi)$, where $\Delta\alpha_{MSHE} = (40 \pm 1)\%$. A variation of this order opens new possibilities for the control of spin currents and thus information flow in spintronics devices. The fact that we observe an even field dependence of the damping modulation with electric currents indicates that the mirror symmetry is broken in $IrMn_3$, which gives rise to the MSHE in this material [16]. In other words, the MSHE is influenced by the contributions of intrinsic Hall conductivities of the domains with opposite chirality of spin [34].

Similar measurements were performed with dc electrical currents applied along the [011] crystallographic direction. The results are similar to the ones shown in Fig. 4(b). It is also worthwhile to note that recently very large anisotropies of the magnetization damping as a function of magnetic field direction with respect to the crystalline orientation have been observed for individual ferromagnetic layers [35]. This differs from the current observation where the magnetic damping of the $Ni_{80}Fe_{20}$ film without any applied electric current is largely independent of the magnetic field orientation as can be seen in Figs. 3(b) and 3(d). In contrast

here, only the electric current dependent part of the magnetization damping shows a large anisotropy.

In summary, we have shown that bilayers of $IrMn_3/Ni_{80}Fe_{20}$ have a strong modulation of electric current induced dampinglike spin torques. The angular magnetic field dependence indicates that these dampinglike torques originate from magnetic spin Hall effects in the $IrMn_3$. This indicates that chiral antiferromagnetic systems, such as $IrMn_3$ can provide additional functionality for electric current control of magnetization dynamics with very different symmetries than what can be expected from conventional spin Hall effects. Thus, this work provides new perspectives for the fundamental understanding of charge- to spin-current conversions in antiferromagnets, as well as new avenues for integrating chiral antiferromagnets into spintronics devices.

*Corresponding author.
joseholanda.papers@gmail.com

[1] V. Baltz, A. Manchon, M. Tsoi, T. Moriyama, T. Ono, and Y. Tserkovnyak, Antiferromagnetic spintronics, Rev. Mod. Phys. **90**, 015005 (2018).

[2] M. B. Jungfleisch, W. Zhang, and A. Hoffmann, Perspectives of antiferromagnetic spintronics, Phys. Lett. A **382**, 865 (2018).

[3] S. M. Rezende, A. Azevedo, and R. L. Rodríguez-Suárez, Introduction to antiferromagnetic magnons, J. Appl. Phys. **126**, 151101 (2019).

[4] J. Zelezný, P. Olejník, A. Hoffmann, and H. Ohno, Spin transport and spin torque in antiferromagnetic devices, Nat. Phys. **14**, 220 (2018).

[5] W. Zhang, M. B. Jungfleisch, W. Jiang, J. E. Pearson, and A. Hoffmann, Spin Hall Effects in Metallic Antiferromagnets, Phys. Rev. Lett. **113**, 196602 (2014).

[6] S. Seki, T. Ideue, M. Kubota, Y. Takagi, M. Nakamura, Y. Kaneko, M. Kawasaki, and Y. Tokura, Thermal Generation

of Spin Current in an Antiferromagnet, Phys. Rev. Lett. **115,** 266601 (2015).

[7] S. M. Wu, W. Zhang, A. KC, P. Borisov, J. E. Pearson, J. S. Jiang, D. Lederman, A. Hoffmann, and A. Bhattacharya, Antiferromagnetic Spin Seebeck Effect, Phys. Rev. Lett. **116,** 097204 (2016).

[8] J. Holanda, D. S. Maior, O. Alves Santos, L. H. Vilela-Leao, J. B. S. Mendes, A. Azevedo, R. L. Rodríguez-Suárez, and S. M. Rezende, Spin Seebeck effect in the antiferromagnet nickel at room temperature, Appl. Phys. Lett. **111,** 172405 (2017).

[9] F. L. A. Machado, P. R. T. Ribeiro, J. Holanda, R. L. Rodríguez-Suárez, A. Azevedo, and S. M. Rezende, Spin-flop transition in the easy-plane antiferromagnet nickel oxide, Phys. Rev. B **95,** 104418 (2017).

[10] P. Wadley *et al.*, Electrical switching of an antiferromagnet, Science **351,** 587 (2016).

[11] H. Saglam, J. C. Rojas-Sanchez, S. Petit, M. Hehn, W. Zhang, J. E. Pearson, S. Mangin, and A. Hoffmann, Independence of spin-orbit torques from the exchange bias direction in $Ni_{81}Fe_{19}$/IrMn bilayers, Phys. Rev. B **98,** 094407 (2018).

[12] J. E. Hirsch, Spin Hall Effect, Phys. Rev. Lett. **83,** 1834 (1999).

[13] S. Nakatsuji, N. Kiyohara, and T. Higo, Large anomalous Hall effect in a non-collinear antiferromagnet at room temperature, Nature (London) **527,** 212 (2015).

[14] A. K. Nayak, J. E. Fischer, Y. Sun, B. Yan, J. Karel, A. C. Komarek, C. Shekhar, N. Kumar, W. Schenelle, J. Kubler, S. S. P. Parkin, and C. Felser, Large anomalous Hall effect driven by a nonvanishing Berry curvature in the non-collinear antiferromagnet $Mn_3Ge$, Sci. Adv. **2,** e1501870 (2016).

[15] R. Shindou and N. Nagaosa, Orbital Ferromagnetism and Anomalous Hall Effect in Antiferromagnets on the Distorted fcc Lattice, Phys. Rev. Lett. **87,** 116801 (2001).

[16] M. Kimata, H. Chen, K. Kondou, S. Sugimoto, P. K. Muduli, M. Ikhlas, Y. Omori, T. Tomita, A. H. MacDonald, S. Nakatsuji, and Y. Otani, Magnetic and magnetic inverse spin Hall effects in a non-collinear antiferromagnet, Nature (London) **565,** 627 (2019).

[17] K. Ando, S. Takahashi, K. Harii, K. Sasage, J. Ieda, S. Maekawa, and E. Saitoh, Electric Manipulation of Spin Relaxation Using the Spin Hall Effect, Phys. Rev. Lett. **101,** 036601 (2008).

[18] L. Liu, T. Moriyama, D. C. Ralph, and R. A. Buhrman, Spin-Torque Ferromagnetic Resonance Induced by the Spin Hall Effect, Phys. Rev. Lett. **106,** 036601 (2011).

[19] L. Szunyogh, B. Lazarovits, L. Udvardi, J. Jackson, and U. Nowak, Giant magnetic anisotropy of the bulk antiferromagnets IrMn and $IrMn_3$ from first principles, Phys. Rev. B **79,** 020403 (2009).

[20] W. Zang, W. Han, S.-H. Yang, Y. Sun, Y. Zhang, B. Yan, and S. S. P. Parkin, Giant facet-dependent spin-orbit torque and spin Hall conductivity in the triangular antiferromagnet $IrMn_3$, Sci. Adv. **2,** e1600759 (2016).

[21] H. Chen, Qian Niu, and A. H. MacDonald, Anomalous Hall Effect Arising From Non-Collinear Antiferromagnetism, Phys. Rev. Lett. **112,** 017205 (2014).

[22] M. Seemann, D. Kodderitzsch, S. Wimmer, and H. Ebert, Symmetry-imposed shape of linear response tensors, Phys. Rev. B **92,** 155138 (2015).

[23] A. Kohn, A. Kovács, R. Fan, G. J. Mclntyre, R. C. C. Ward, and J. P. Goff, The antiferromagnetic structures of $IrMn_3$ and their influence on exchange-bias, Sci. Rep. **3,** 2412 (2013).

[24] J. Holanda, O. Alves Santos, R. L. Rodríguez-Suárez, A. Azevedo, and S. M. Rezende, Simultaneous spin pumping and spin Seebeck experiments with thermal control of the magnetic damping in bilayers of yttrium iron garnet and heavy metals: YIG/Pt and YIG/IrMn, Phys. Rev. B **95,** 134432 (2017).

[25] T. L. Gilbert, A phenomenological theory of damping in ferromagnetic materials, IEEE Trans. Magn. **40,** 3443 (2004).

[26] W. Zhang, W. Han, X. Jiang, S.-H. Yang, and S. S. P. Parkin, Role of transparency of platinum-ferromagnet interfaces in determining the intrinsic magnitude of the spin Hall effect, Nat. Phys. **11,** 496 (2015).

[27] M. Tsunoda, T. Sato, T. Hashimoto, and M. Takahashi, Exchange anisotropy of polycrystalline Mn-Ir/Co-Fe bilayers enlarged by long-time annealing, Appl. Phys. Lett. **84,** 5222 (2004).

[28] C. G. Shull and M. K. Wilkinson, Neutron diffraction studies of various transition elements, Rev. Mod. Phys. **25,** 100 (1953).

[29] S. Maekawa, S. O. Valenzuela, E. Saitoh, and T. Kimura, *Spin Current* (Oxford Univ. Press, Oxford, 2012).

[30] W. T. Soh, Y. Yeow, X. Zhong, and C. K. Ong, Inverse spin Hall effect of antiferromagnetic MnIr in exchange biased NiFe/MnIr films, J. Phys. D **48,** 345002 (2015).

[31] A. Tsukahara, Y. Ando, Y. Kitamura, H. Emoto, E. Shikoh, M. P. Delmo, T. Shinjo, and M. Shiraishi, Self-induced inverse spin Hall effect in permalloy at room temperature, Phys. Rev. B **89,** 235317 (2014).

[32] V. Hemmati, M. L. Plumer, J. P. Whitehead, and B. W. Southern, Monte Carlo simulations of magnetic ordering in the fcc Kagome lattice, Phys. Rev. B **86,** 104419 (2012).

[33] Y. Liu, Y. Liu, M. Chen, S. Srivastava, P. He, K. L. Teo, T. Phung, S.-H. Yang, and H. Yang, Current-Induced Out-of-Plane Spin Accumulation on the (001) Surface of the $IrMn_3$ Antiferromagnet, Phys. Rev. Applied **12,** 064046 (2019).

[34] Y. Zhang, Y. Sun, H. Yang, J. Zelezny, S. S. P. Parkin, C. Felser, and B. Yan, Strong anisotropic anomalous Hall effect and spin Hall effect in the chiral antiferromagnetic compounds $Mn_3X$ ($X$ = Ge, Sn, Ga, Ir, Rh, and Pt), Phys. Rev. B **95,** 075128 (2017).

[35] Y. Li, F. Zeng, S. S.-L. Zhang, H. Shin, H. Saglam, V. Karakas, O. Ozatay, J. E. Pearson, O. G. Heinonen, Y. Wu, A. Hoffmann, and W. Zhang, Giant Anisotropy of Gilbert Damping in Epitaxial CoFe Films, Phys. Rev. Lett. **122,** 117203 (2019).